Modeling of Far-Field Quantum Coherence by Dielectric Bodies Based on the Volume Integral Equation Method

Chengnian Huang, *Student Member, IEEE*, Hangyu Ge, Yijia Cheng, Zi He, *Senior Member, IEEE*, Feng Liu, and Wei E. I. Sha, *Fellow, IEEE*

***Abstract*—The Hong–Ou–Mandel (HOM) effect is a hallmark of nonclassical two-photon interference. This article develops a unified theory–numerics framework to compute angle-resolved far-field two-photon correlations from arbitrary lossless dielectric scatterers. We describe the input–output relation using a multichannel scattering formulation that maps two populated incident channels to two selected far-field detection modes, yielding a compact two-channel transfer relation for the second-order correlation function and time-domain coincidence counts. The required transfer coefficients are extracted from classical far-field complex amplitudes computed by a fast Fourier transform (FFT)-accelerated volume integral equation (VIE) solver, avoiding perfectly matched layers (PMLs) and near-to-far-field postprocessing. The method is validated against analytical results for dielectric spheres and demonstrated on a polarization-converting Pancharatnam–Berry-phase (PBP) metasurface, revealing strong angular dependence of quantum interference and its direct impact on HOM-dip visibility. The framework provides an efficient and physically transparent tool for structure-dependent quantum-correlation analysis, with potential applications in scatterers-enabled quantum state engineering and quantum inverse design.**

***Index Terms*—Coincidence counts, far-field scattering, Hong–Ou–Mandel (HOM) effect, second-order correlation function, two-photon interference, volume integral equation (VIE).**

I. Introduction

OVER the past few years, quantum information [1], [2], quantum computing [3], and quantum optics [4] have advanced rapidly, motivating accurate theoretical models and scalable numerical solvers for quantum electromagnetic systems. Within macroscopic quantum electrodynamics (QED) [5], [6], a wide range of effects including spontaneous emission in dielectrics [7], [8], [9], [10], Casimir forces [11], artificial atoms [12], few-photon interference in passive lossless devices [13], and quantum–optical metamaterials [14] can be treated in a unified field-quantization framework.

A central theme in these platforms is scattering-induced quantum interference, which enables controlled manipulation of photon statistics and correlations [15]. For single-photon excitation, the detected intensity pattern follows the corresponding classical wave solution for the same input mode. In contrast, under multiphoton excitation, interference between Fock-state probability amplitudes [16], [17], [18] yields genuinely nonclassical correlations that do not admit a classical description [19]. A canonical example is the Hong–Ou–Mandel (HOM) effect [20], [21]: two indistinguishable photons impinging on a balanced beam splitter exhibit suppressed coincidences due to destructive two-photon interference.

To predict such nonclassical scattering phenomena, both analytical quantization schemes and numerical solvers have been explored. Separation-of-variables quantization has been developed for spherically layered systems and parabolic mirrors [22], [23], and far-field correlation functions of canonical dielectric objects can be derived analytically in special geometries [24]. More generally, Green's-function-based macroscopic QED provides a versatile route for treating structured and inhomogeneous environments [25], [26], [27].

For arbitrary inhomogeneous and lossless dielectric systems, a common computational route is to expand the quantized field operators on a set of numerical (or quasinormal) modes and to promote the classical modal amplitudes to operators by associating them with creation and annihilation operators [4], [28], [29], [30]. For example, characteristic-mode theory [31], [32], [33], [34], [35], [36] has been used to analyze scattering-induced entanglement for perfectly conducting bodies [15]. Differential-equation-based solvers [37], [38], [39] have also been employed to compute normal modes and study few-photon interference [5], [40], [41]. However, for large-scale far-field scattering problems, these methods may suffer from numerical dispersion and the need for artificial boundary truncation, which can complicate phase-accurate far-field correlation predictions.

Integral-equation formulations offer an attractive alternative because they leverage analytical Green's functions that satisfy radiation conditions and thus preserve phase propagation exactly. Recent advances by Forestiere and Miano [42], Forestiere et al. [43], and Miano et al. [44] established rigorous integral formulations for macroscopic QED in dispersive

Received 17 August 2025; revised 31 January 2026; accepted 30 March 2026. Date of publication 17 April 2026; date of current version 9 July 2026. This work was supported in part by the National Natural Science Foundation of China under Grant 61975177, Grant U20A20164, and Grant U21A6006; in part by the National Key Research and Development Program of China under Grant 2023YFB2806000 and Grant 2022YFA1204700; and in part by Zhejiang Provincial Natural Science Foundation of China under Grant LR25F040001. *(Corresponding author: Wei E. I. Sha.)*

Chengnian Huang, Hangyu Ge, Yijia Cheng, Feng Liu, and Wei E. I. Sha are with the College of Information Science and Electronic Engineering, Zhejiang University, Hangzhou 310027, China (e-mail: weisha@zju.edu.cn).

Zi He is with the Department of Communication Engineering, Nanjing University of Science and Technology, Nanjing 210094, China.

Digital Object Identifier 10.1109/TAP.2026.3683145

dielectric objects. In the lossless setting considered here, radiated observables admit an efficient representation in terms of propagating outgoing channels (e.g., spherical-wave modes), while evanescent components remain confined to the near field and carry no net radiated power. This viewpoint motivates a direct connection between classical far-field scattering amplitudes and quantum photodetection correlations. Building on the framework in [45], normally ordered photodetection correlation functions can be expressed through classical field quantities, enabling angle-dependent two-photon interference (including HOM-type features) to be evaluated from the far-field responses to independently incident single-photon beams.

In this article, we study the far-field interference produced when two independent single photons illuminate an arbitrary lossless dielectric object and are correlation-detected at two observation angles. The objective is to compute the second-order normalized correlation function $g^{(2)}$ in both the frequency and time domains by integrating macroscopic quantum theory with a scalable computational electromagnetics (CEM) solver. Specifically, we adopt a volume integral equation (VIE) formulation in which analytical dyadic Green's functions enforce the radiation condition at infinity and avoid numerical dispersion.

For each incident channel, the VIE solver computes the induced polarization currents, from which the far-field response is evaluated directly. This eliminates the need for perfectly matched layers (PMLs) or near-to-far-field postprocessing typically required by differential-equation solvers. Moreover, fast Fourier transform (FFT)-accelerated matrix–vector multiplication (MVM) and block preconditioning enable large-scale simulations of dielectric nanostructures with practical computational cost [46].

The main contributions are summarized as follows.

1) We develop a unified VIE–dyadic-Green's-function framework that links classical far-field scattering amplitudes to quantum second-order correlation functions for two-photon interference.
2) The proposed approach avoids heavy normal-mode expansions and mitigates convergence and boundary-related issues commonly encountered in quantum FDTD or mode-based methods, improving efficiency and numerical robustness for large-scale far-field problems.
3) We connect frequency-domain $g^{(2)}$ maps to time-domain coincidence curves $\tilde{N}_c(\delta\tau)$, enabling direct prediction of experimentally observable HOM-type interference signatures.

The remainder of this article is organized as follows. Section II reviews the quantum-field formalism and derives $g^{(2)}$ in the frequency domain as well as the normalized coincidence function in the time domain. Section III presents two numerical examples: a dielectric sphere and a polarization-converting metasurface. Section IV concludes this article and discusses future directions.

II. Theory

In the classical world, observable physical quantities such as position or velocity are deterministic. However, due to intrinsic quantum fluctuations, the state of a photon in the microscopic regime must be described by a quantum state vector. For a (nonentangled) single photon prepared as a wavepacket [47], the corresponding state can be expressed as a coherent superposition of single-photon Fock states

$$|\Psi\rangle = \sum_{n=1}^{N} \phi_n |1\rangle_n = \sum_{n=1}^{N} \phi_n \hat{a}_n^\dagger |0\rangle, \quad \sum_{n=1}^{N} |\phi_n|^2 = 1 \tag{1}$$

where ϕ_n denotes the probability amplitude of mode n, incorporating the spectral (and, if needed, directional/polarization) profile of the wavepacket; $\hat{a}_n^\dagger$ is the creation operator; and $|0\rangle$ denotes the vacuum state. The discrete summation over N modes represents a discretization of the wavepacket over an orthonormal set of free-space modes (channels).

If two photons are independent (nonentangled), a convenient two-photon input state can be written as

$$|\Psi\rangle_{12} = \left(\sum_{n=1}^{N} \phi_{1n}\hat{a}_n^\dagger\right)\left(\sum_{m=1}^{N} \phi_{2m}\hat{a}_m^\dagger\right)|0\rangle \tag{2}$$

$$\sum_n |\phi_{1n}|^2 = \sum_m |\phi_{2m}|^2 = 1 \tag{3}$$

where ϕ_{1n} and ϕ_{2m} describe the two single-photon wavepackets.

Similarly, the classical field quantities in Maxwell's equations are elevated to field operators in the quantum formalism. The electric-field operator is conventionally decomposed into the positive- and negative-frequency components

$$\hat{\mathbf{E}}(\mathbf{r},t) = \hat{\mathbf{E}}^{(+)}(\mathbf{r},t) + \hat{\mathbf{E}}^{(-)}(\mathbf{r},t). \tag{4}$$

These components can be expanded over an orthonormal set of free-space modes (channels) as

$$\begin{aligned}\hat{\mathbf{E}}^{(+)}(\mathbf{r},t) &= \sum_n C\sqrt{\omega_n}\mathbf{E}_n(\mathbf{r})\,\hat{a}_n(t)\\ &= \sum_n C\sqrt{\omega_n}\mathbf{E}_n(\mathbf{r})\,e^{-i\omega_n t}\hat{a}_n \end{aligned}\tag{5}$$

$$\begin{aligned}\hat{\mathbf{E}}^{(-)}(\mathbf{r},t) &= \sum_n C\sqrt{\omega_n}\mathbf{E}_n^*(\mathbf{r})\,\hat{a}_n^\dagger(t)\\ &= \sum_n C\sqrt{\omega_n}\mathbf{E}_n^*(\mathbf{r})\,e^{i\omega_n t}\hat{a}_n^\dagger \end{aligned}\tag{6}$$

where ω_n is the mode frequency, $\mathbf{E}_n(\mathbf{r})$ is the corresponding (normalized) mode profile, and C is a normalization constant fixed by the chosen quantization convention. $\hat{a}_n$ and $\hat{a}_n^\dagger$ are the annihilation and creation operators, respectively.

To explore the quantum characteristics of electromagnetic fields, we consider the probability of joint photodetection, which is mathematically modeled by correlation functions. The photodetection scheme with two detectors located at $\mathbf{r}_1$ and $\mathbf{r}_2$ is illustrated in Fig. 1.

The first-order correlation function, proportional to the single-photon detection probability at position $\mathbf{r}_1$ with polarization $\mathbf{e}_a$, is defined as

$$G_a^{(1)}(\mathbf{r}_1,t) = \langle\Psi|\hat{E}_a^{(-)}(\mathbf{r}_1,t)\,\hat{E}_a^{(+)}(\mathbf{r}_1,t)\,|\Psi\rangle \tag{7}$$

where $\hat{E}_a^{(-)}(\mathbf{r}_1,t) = \hat{\mathbf{E}}^{(-)}(\mathbf{r}_1,t)\cdot\mathbf{e}_a = [\hat{E}_a^{(+)}(\mathbf{r}_1,t)]^\dagger$ is the projection of the negative-frequency field operator onto the polarization vector.

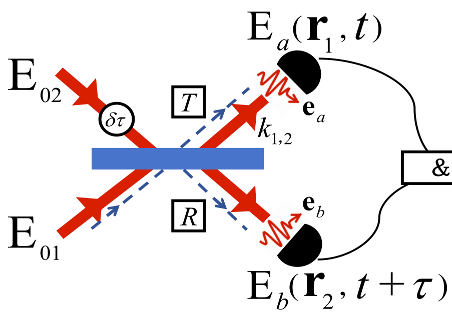

Fig. 1. Schematic of the photon detection setup, where two detectors are placed at positions $\mathbf{r}_1$ and $\mathbf{r}_2$, with polarization detection directions $\mathbf{e}_a$ and $\mathbf{e}_b$, respectively.

The second-order correlation function, corresponding to fourth-order field interference, yields the joint probability to detect one photon at $\mathbf{r}_1$ with polarization $\mathbf{e}_a$ and another photon at $\mathbf{r}_2$ with polarization $\mathbf{e}_b$

$$G^{(2)}_{ab}(\mathbf{r}_1, \mathbf{r}_2, t) = \langle \Psi | \hat{E}^-_a(\mathbf{r}_1, t)\, \hat{E}^-_b(\mathbf{r}_2, t) \times \hat{E}^+_b(\mathbf{r}_2, t)\, \hat{E}^+_a(\mathbf{r}_1, t) | \Psi \rangle. \tag{8}$$

To assess the degree of quantum coherence, the normalized second-order correlation function [48], [49] is introduced

$$g^{(2)}_{ab}(\mathbf{r}_1, \mathbf{r}_2, t) = \frac{G^{(2)}_{ab}(\mathbf{r}_1, \mathbf{r}_2, t)}{G^{(1)}_a(\mathbf{r}_1, t)\, G^{(1)}_b(\mathbf{r}_2, t)}. \tag{9}$$

A. Correlation Function in the Frequency Domain

For a linear, time-invariant, and lossless dielectric scatterer, the input–output relation of the quantized field can be formulated as a unitary mapping between complete orthonormal sets of asymptotic modes (channels). We start from a plane-wave basis (including polarization) for the incident field, with annihilation operators $\{\hat{a}_\alpha\}$ satisfying the canonical commutation relations $[\hat{a}_\alpha, \hat{a}^\dagger_\beta] = \delta_{\alpha\beta}$. For far-field analysis, it is convenient to express the same free-space field in an incoming spherical-wave basis $\{\hat{b}^{(\mathrm{in})}_\mu\}$. These two complete bases are related by a frequency-dependent unitary transformation

$$\hat{b}^{(\mathrm{in})}_\mu = \sum_\alpha U_{\mu\alpha}\, \hat{a}_\alpha, \quad U^\dagger U = I \tag{10}$$

which preserves commutation relations.

The scatterer maps incoming channels into outgoing channels through the scattering matrix

$$\hat{b}^{(\mathrm{out})}_\nu = \sum_\mu S_{\nu\mu}\, \hat{b}^{(\mathrm{in})}_\mu. \tag{11}$$

For a lossless object, the full multichannel matrix S is unitary ($S^\dagger S = I$), ensuring preservation of the bosonic commutators for the output operators $\{\hat{b}^{(\mathrm{out})}_\nu\}$.

In this work, only two independent single-photon wavepackets are injected into two selected input channels (denoted as 1 and 2), while all other input channels are in the vacuum state. Because the photodetection correlations considered here are normally ordered, vacuum input channels contribute zero to the relevant expectation values and can therefore be omitted when evaluating $G^{(1)}$ and $G^{(2)}$.

Under a narrowband approximation (the system response varies negligibly over the photon bandwidth around ω_0),[1] the detected positive-frequency field operators at the two detectors can be written as linear combinations of the two excited input operators, with the corresponding transfer coefficients treated as approximately frequency-independent over that bandwidth

$$\hat{E}^{(+)}_a(\mathbf{r}_1, t) = \sum_{j=1}^{2} T_{aj}\, e^{-i\omega_0 t}\, \hat{a}_j \tag{12}$$

$$\hat{E}^{(+)}_b(\mathbf{r}_2, t) = \sum_{j=1}^{2} T_{bj}\, e^{-i\omega_0 t}\, \hat{a}_j \tag{13}$$

where T_{aj} and T_{bj} are complex transfer coefficients that incorporate the scatterer response, propagation, and polarization projection. These coefficients are extracted from the full-wave (VIE-FFT) solution of the corresponding classical scattering problem. Note that the 2×2 matrix formed by $\{T_{aj}, T_{bj}\}$ is a projection of the full multichannel mapping onto two selected detection modes and is therefore not generally unitary, because power may scatter into unobserved output channels; unitarity holds only for the full multichannel S-matrix.

Equivalently, keeping explicit mode functions as in (5)–(6), one may write

$$\hat{E}^+_a(\mathbf{r}_1, t) = C\sqrt{\omega_{k_1}}\, E_{ak_1}(\mathbf{r}_1)\, e^{-i\omega_{k_1} t}\, \hat{a}_1 + C\sqrt{\omega_{k_2}}\, E_{ak_2}(\mathbf{r}_1)\, e^{-i\omega_{k_2} t}\, \hat{a}_2 \tag{14}$$

$$\hat{E}^+_b(\mathbf{r}_2, t) = C\sqrt{\omega_{k_1}}\, E_{bk_1}(\mathbf{r}_2)\, e^{-i\omega_{k_1} t}\, \hat{a}_1 + C\sqrt{\omega_{k_2}}\, E_{bk_2}(\mathbf{r}_2)\, e^{-i\omega_{k_2} t}\, \hat{a}_2. \tag{15}$$

The negative-frequency components are followed by Hermitian conjugation.

To incorporate a finite numerical aperture (NA), we define an aperture-collected field operator

$$\hat{E}^{(+)}_{a,\mathrm{NA}}(t) = \int_{\mathrm{NA}} W_a(\mathbf{k})\, \hat{E}^{(+)}(\mathbf{k}, t)\, d^2\mathbf{k} \tag{16}$$

and similarly for $\hat{E}^{(+)}_{b,\mathrm{NA}}(t)$, where $W(\mathbf{k})$ is the angular sensitivity function of the detector. The experimentally relevant quantities are then $G^{(1)}_{a,\mathrm{NA}} = \langle \hat{E}^{(-)}_{a,\mathrm{NA}} \hat{E}^{(+)}_{a,\mathrm{NA}} \rangle$, $G^{(2)}_{ab,\mathrm{NA}} = \langle \hat{E}^{(-)}_{a,\mathrm{NA}} \hat{E}^{(-)}_{b,\mathrm{NA}} \hat{E}^{(+)}_{b,\mathrm{NA}} \hat{E}^{(+)}_{a,\mathrm{NA}} \rangle$, followed by $g^{(2)}_{ab,\mathrm{NA}} = G^{(2)}_{ab,\mathrm{NA}} / (G^{(1)}_{a,\mathrm{NA}} G^{(1)}_{b,\mathrm{NA}})$. Note that in our numerical implementation, under the narrowband approximation, the spatial integration over the NA is not explicitly performed. Instead, by approximating the collected signal through contributions from specific discrete modes at the center of the detection angles, the substitution of [(12) and (13)] into (9) yeilds

$$g^{(2)}_{ab} = \frac{\sum_{m,n,p,q\in\{1,2\}} T^*_{am} T^*_{bn} T_{bp} T_{aq} \left\langle \Psi \left| \hat{a}^\dagger_m \hat{a}^\dagger_n \hat{a}_p \hat{a}_q \right| \Psi \right\rangle}{\sum_{m,q\in\{1,2\}} T^*_{am} T_{aq} \langle \Psi | \hat{a}^\dagger_m \hat{a}_q | \Psi \rangle \sum_{n,p\in\{1,2\}} T^*_{bn} T_{bp} \langle \Psi | \hat{a}^\dagger_n \hat{a}_p | \Psi \rangle}. \tag{17}$$

For the two-single-photon Fock input $|1_1, 1_2\rangle = \hat{a}^\dagger_1 \hat{a}^\dagger_2 |0\rangle$, the fourth-order expectation $\langle \hat{a}^\dagger_m \hat{a}^\dagger_n \hat{a}_p \hat{a}_q \rangle$ vanishes whenever any

[1]Regarding the source characteristics, the incident single-photon wavepacket generated by high-performance quantum emitters is assumed, such as the wavelength-tunable semiconductor quantum dots recently demonstrated in [50].

annihilation operator attempts to remove two photons from the same occupied mode (since $n_1 = n_2 = 1$). Therefore, only terms that annihilate one photon from each occupied mode survive, resulting in the direct and exchange two-photon paths and their interference. If $\omega_{k_1} \neq \omega_{k_2}$, the cross terms acquire a beating phase $e^{-i(\omega_{k_1}-\omega_{k_2})t}$ and vanish under experimental time averaging unless the two wavepackets are sufficiently overlapped in frequency (i.e., effectively indistinguishable). In the degenerate (or effectively narrowband) case $\omega_{k_1} \approx \omega_{k_2}$, this explicit time dependence cancels in $g^{(2)}$.

In the degenerate/narrowband case and using (14)–(15), the normalized correlation reduces to a compact far-field form

$$g_{ab}^{(2)}(\mathbf{r}_1, \mathbf{r}_2) = \frac{\omega_{k_1}\omega_{k_2}|E_{ak_1}(\mathbf{r}_1)\, E_{bk_2}(\mathbf{r}_2) + E_{ak_2}(\mathbf{r}_1)\, E_{bk_1}(\mathbf{r}_2)|^2}{\left(\sum_{l=1,2}\omega_{k_l}|E_{ak_l}(\mathbf{r}_1)|^2\right)\left(\sum_{l=1,2}\omega_{k_l}|E_{bk_l}(\mathbf{r}_2)|^2\right)}. \tag{18}$$

The numerator contains the classical-like contributions from the direct and exchange paths and, crucially, the cross terms that arise from quantum indistinguishability. When the two photons are perfectly indistinguishable, these cross terms yield maximum two-photon interference (e.g., the HOM suppression of coincidences); when they are fully distinguishable, the cross terms vanish, and the coincidence reduces to an incoherent sum of independent intensities. Ultimately, for the two-single-photon Fock input considered here and the above normalization, the resulting $g^{(2)}$ is bounded between 0 and 1, reflecting the antibunching associated with single-photon excitation [51], [52]. In contrast, incoherent classical emitters can exhibit autocorrelation values exceeding unity under the conditions $\mathbf{r}_1 = \mathbf{r}_2$ and $\mathbf{e}_a = \mathbf{e}_b$ [53].

B. Normalized Coincidence Number Function in the Time Domain

To model experimentally observed coincidence measurements in the time domain, we derive the expected coincidence number N_c as a function of an externally controlled optical path delay $\delta\tau$, following the standard treatment in [20]. The delay $\delta\tau$ represents a controllable input delay, effectively shifting the arrival time of one wavepacket relative to the other.

1) Beam-Splitter Reference Formulation: We first recall the phase-asymmetric beam-splitter model. Let $\hat{E}_{01}^{(+)}(t)$ and $\hat{E}_{02}^{(+)}(t)$ denote the incident positive-frequency field operators associated with the two input channels. An adjustable delay $\delta\tau$ is applied to the second input wavepacket. The output fields at the two detectors are then written as linear combinations of the delayed inputs

$$\hat{E}_a^{(+)}(\mathbf{r}_1, t) = \sqrt{T}\,\hat{E}_{01}^{(+)}(t) + i\sqrt{R}\,\hat{E}_{02}^{(+)}(t+\delta\tau) \tag{19}$$

$$\hat{E}_b^{(+)}(\mathbf{r}_2, t+\tau) = \sqrt{T}\,\hat{E}_{02}^{(+)}(t+\tau) + i\sqrt{R}\,\hat{E}_{01}^{(+)}(t+\tau-\delta\tau) \tag{20}$$

where $\tau \equiv t_b - t_a$ is the detection-time difference between the two detectors. Note that $\delta\tau$ is a controlled input delay applied to one wavepacket, whereas τ is the random detection time difference over which coincidence events are accumulated.

The second-order correlation function $G_{ab}^{(2)}(\tau; \delta\tau)$ is obtained from (8) by substituting the field operators above. For two independent single-photon wavepackets with spectral amplitude functions $\phi_1(\omega)$ and $\phi_2(\omega)$, the key quantity governing two-photon interference is the wavepacket overlap function

$$h(\tau) = \int_{-\infty}^{\infty} d\omega\, \phi_1^*(\omega)\, \phi_2(\omega)\, e^{-i\omega\tau}. \tag{21}$$

For identical Gaussian spectra centered at ω_0 with rms bandwidth $1/\sigma$, one obtains (up to an irrelevant global phase)

$$h(\tau) = \exp\left(-\frac{\tau^2}{2\sigma^2}\right) e^{-i\omega_0\tau} \tag{22}$$

and consequently $|h(\tau)|^2 = \exp(-\tau^2/\sigma^2)$.

With this definition, the beam-splitter correlation function takes the standard HOM form

$$\begin{aligned} G_{ab}^{(2)}(\tau; \delta\tau) = K\big[&T^2|h(\tau)|^2 + R^2|h(2\delta\tau-\tau)|^2 \\ &- RT\, h^*(\tau)\, h(2\delta\tau-\tau) \\ &- RT\, h(\tau)\, h^*(2\delta\tau-\tau)\big] \end{aligned} \tag{23}$$

where K is a positive constant determined by the overall normalization and detector response. In typical coincidence experiments, the integration window is much longer than the coherence time, so that the expected coincidence number is

$$N_c(\delta\tau) = \int_{-\infty}^{\infty} G_{ab}^{(2)}(\tau; \delta\tau)\, d\tau. \tag{24}$$

2) Extension to an Arbitrary Lossless Scattering Environment: We now generalize the above beam-splitter model to an arbitrary (lossless) scattering environment computed by the full-wave solver. The environment determines how the two incident wavepackets are mapped into far-field observation directions and polarizations at $\mathbf{r}_1$ and $\mathbf{r}_2$. In the narrowband regime, the detector-projected far-field amplitudes at ω_0 play the role of complex transfer coefficients. Specifically, the two indistinguishable two-photon detection paths are associated with the complex amplitudes

$$A_{\text{dir}} = E_{ak_1}(\mathbf{r}_1)\, E_{bk_2}(\mathbf{r}_2), \quad A_{\text{ex}} = E_{ak_2}(\mathbf{r}_1)\, E_{bk_1}(\mathbf{r}_2) \tag{25}$$

evaluated at $\omega_{k_1} = \omega_{k_2} = \omega_0$, while the temporal/spectral profile of the wavepackets is retained through $h(\cdot)$. This operator-level mapping from input channels to far-field detection modes follows from the Heisenberg evolution in linear media and can be formulated via Green's-function quantization in inhomogeneous environments [54], [55], [56].

Under this framework, the time-resolved correlation function can be written as

$$\begin{aligned} G_{ab}^{(2)}(\tau; \delta\tau) = K\big[&|A_{\text{dir}}|^2\,|h(\tau)|^2 + |A_{\text{ex}}|^2\,|h(2\delta\tau-\tau)|^2 \\ &+ A_{\text{dir}}A_{\text{ex}}^*\, h(\tau)\, h^*(2\delta\tau-\tau) \\ &+ A_{\text{dir}}^*A_{\text{ex}}\, h^*(\tau)\, h(2\delta\tau-\tau)\big]. \end{aligned} \tag{26}$$

The above equation reduces to (23) for an ideal beam splitter when $A_{\text{dir}} = T$ and $A_{\text{ex}} = -R$.

3) Normalized Coincidence Number: Experimentally, one is typically interested in the coincidence number integrated over τ. Using (24) and (26), we define the normalized coincidence number $\tilde{N}_c(\delta\tau)$ such that $\tilde{N}_c(\delta\tau) \to 1$ as $|\delta\tau| \to \infty$

$$\tilde{N}_c(\delta\tau) = \frac{N_c(\delta\tau)}{D_c} \tag{27}$$

where the normalization factor D_c is chosen as the integral of the product of two terms (i.e., the large-delay limit of the coincidence rate)

$$D_c = \int_{-\infty}^{\infty} G_a^{(1)}(\tau;\delta\tau)\, G_b^{(1)}(\tau;\delta\tau)\, d\tau \tag{28}$$

so that $\tilde{N}_c(\delta\tau)$ is dimensionless and asymptotically approaches unity.

Carrying out the τ-integration in (26) yields a compact decomposition

$$\tilde{N}_c(\delta\tau) = \frac{N_1(\delta\tau) + N_2(\delta\tau) + N_3(\delta\tau) + N_4(\delta\tau)}{D_c} \tag{29}$$

with

$$N_1(\delta\tau) = |A_{\mathrm{dir}}|^2 \int_{-\infty}^{\infty} |h(\tau)|^2\, d\tau \tag{30}$$

$$N_2(\delta\tau) = |A_{\mathrm{ex}}|^2 \int_{-\infty}^{\infty} |h(2\delta\tau - \tau)|^2\, d\tau \tag{31}$$

$$N_3(\delta\tau) = A_{\mathrm{dir}} A_{\mathrm{ex}}^* \int_{-\infty}^{\infty} h(\tau)\, h^*(2\delta\tau - \tau)\, d\tau \tag{32}$$

$$N_4(\delta\tau) = A_{\mathrm{dir}}^* A_{\mathrm{ex}} \int_{-\infty}^{\infty} h^*(\tau)\, h(2\delta\tau - \tau)\, d\tau. \tag{33}$$

Moreover, for identical Gaussian spectra (22), one obtains the standard HOM envelope

$$\int_{-\infty}^{\infty} h(\tau)\, h^*(2\delta\tau - \tau)\, d\tau \;\propto\; \exp\left(-\frac{\delta\tau^2}{\sigma^2}\right) \tag{34}$$

so that the dip width is governed by the coherence time, represented by the Gaussian width parameter σ. It should be explicitly clarified that σ is an assumed constant, independent of the monochromatic frequency-domain scattering results. This parameter is employed solely to enable the transition from monochromatic data to a temporal profile; thus, the resulting coincidence curves do not represent a full broadband frequency-domain simulation, but rather a theoretical visualization based on the assumed temporal envelope.

The temporal envelope of the excitation pulses thus defines the coherence time of the generated photons and determines the characteristic width of the interference curve. In this work, we emphasize the comparative behavior of $\tilde{N}_c(\delta\tau)$ across different scattering environments; the absolute temporal scale can be mapped to a specific experimental implementation through the pulse bandwidth and detector timing response. Accordingly, σ is assigned as a dimensionless value consistent with this normalized temporal scale.

C. Numerical Method

To obtain the far-field complex amplitudes at the detection directions for a given frequency, we employ a VIE solver accelerated by FFT in this work. Following the electromagnetic equivalence principle, the dielectric scatterer occupying a volume V is embedded in a homogeneous background (vacuum), and the scattering effect is represented by an induced volumetric polarization current inside V. In the frequency domain ($e^{-i\omega t}$ convention), the polarization current is defined as

$$\mathbf{J}^{\mathrm{s}}(\mathbf{r}) = -i\omega\left[\varepsilon(\mathbf{r}) - \varepsilon_0\right]\mathbf{E}^{\mathrm{tot}}(\mathbf{r}), \quad \mathbf{r} \in V \tag{35}$$

where $\varepsilon(\mathbf{r})$ is the (possibly piecewise-constant) permittivity distribution and $\mathbf{E}^{\mathrm{tot}}$ is the total electric field. The scattered field produced by $\mathbf{J}^{\mathrm{s}}$ is expressed via the free-space dyadic Green's function $\overleftrightarrow{\mathbf{G}}$ as

$$\mathbf{E}^{\mathrm{sca}}(\mathbf{r}) = i\omega\mu_0 \int_V \overleftrightarrow{\mathbf{G}}(\mathbf{r},\mathbf{r}') \cdot \mathbf{J}^{\mathrm{s}}(\mathbf{r}')\, dv' \tag{36}$$

and the total field satisfies $\mathbf{E}^{\mathrm{tot}} = \mathbf{E}^{\mathrm{inc}} + \mathbf{E}^{\mathrm{sca}}$. Substituting (35) and (36) yields a VIE in terms of the unknown current $\mathbf{J}^{\mathrm{s}}$

$$\begin{aligned} -\frac{\mathbf{J}^{\mathrm{s}}(\mathbf{r})}{i\omega(\varepsilon(\mathbf{r}) - \varepsilon_0)} - i\omega\mu_0 \int_V \overleftrightarrow{\mathbf{G}}(\mathbf{r},\mathbf{r}') \\ \cdot \mathbf{J}^{\mathrm{s}}(\mathbf{r}')\, dv' = \mathbf{E}^{\mathrm{inc}}(\mathbf{r}), \mathbf{r} \in V \end{aligned} \tag{37}$$

where the free-space dyadic Green's function is

$$\overleftrightarrow{\mathbf{G}}(\mathbf{r},\mathbf{r}') = \left(\overleftrightarrow{\mathbf{I}} + \frac{1}{k_0^2}\nabla\nabla\right)\frac{e^{ik_0|\mathbf{r}-\mathbf{r}'|}}{4\pi|\mathbf{r}-\mathbf{r}'|} \tag{38}$$

with $k_0 = \omega\sqrt{\mu_0\varepsilon_0}$ and ε_0 and μ_0 are the permittivity and permeability of free space, respectively.

We discretize (37) using the method of moments (MoM) [57]. The unknown volumetric current is expanded on a uniform hexahedral grid using rooftop (piecewise linear) basis functions oriented along the three Cartesian directions

$$\mathbf{J}^{\mathrm{s}}(\mathbf{r}) = \sum_{i\in\{x,y,z\}} \hat{\mathbf{p}}_i \sum_{k=1}^{N_1}\sum_{m=1}^{N_2}\sum_{n=1}^{N_3} J_i(k,m,n)\, T_{kmn}^{(i)}(\mathbf{r}) \tag{39}$$

where $\hat{\mathbf{p}}_i$ denotes the unit vector along direction i, $J_i(k,m,n)$ are the expansion coefficients, and $T_{kmn}^{(i)}$ are the volumetric rooftop basis functions. Pulse (piecewise-constant) testing functions are used in a Galerkin-like collocation manner. The rooftop expansion is advantageous because it enforces appropriate intercell continuity (notably the normal flux continuity across shared faces), improving numerical stability and accuracy for volumetric formulations.

For an arbitrary geometry, a structured (uniform) voxelization leads to a discrete convolution structure between the current unknowns and the Green's function kernel. Consequently, MVMs can be accelerated by the FFT, reducing the computational cost from $\mathcal{O}(N^2)$ to approximately $\mathcal{O}(N\log N)$ for large-scale problems. The resulting linear system can be efficiently solved using the bi-conjugate gradient stabilized (BiCGStab) iterative method [58]. For large-scale scatterers, additional efficiency gains can be achieved via block preconditioners and parallel computing [46].

Once the polarization current is obtained, the far-field scattered electric field can be evaluated using the radiation-zone asymptotic form of the dyadic Green's function. The scattered far-field amplitude in the observation direction $\hat{\mathbf{r}}$ can be written as

$$\mathbf{E}_{\infty}^{\mathrm{sca}}(\hat{\mathbf{r}}) = C_{\infty} \int_V \left[\hat{\mathbf{r}} \times \left(\mathbf{J}^{\mathrm{s}}(\mathbf{r}') \times \hat{\mathbf{r}}\right)\right] e^{-ik_0\hat{\mathbf{r}}\cdot\mathbf{r}'}\, d\mathbf{r}' \tag{40}$$

where C_{∞} is a frequency-dependent proportionality constant determined by the chosen far-field normalization and $\hat{\mathbf{r}}$ denotes the unit vector in the observation direction. The detector-projected complex amplitudes used in the correlation analysis are then obtained as

$$E_{ak}(\mathbf{r}_1) = \mathbf{e}_a \cdot \mathbf{E}_{\infty}^{\mathrm{tot}}(\hat{\mathbf{r}}_1;\omega_k), \quad E_{bk}(\mathbf{r}_2) = \mathbf{e}_b \cdot \mathbf{E}_{\infty}^{\mathrm{tot}}(\hat{\mathbf{r}}_2;\omega_k) \tag{41}$$

where $\mathbf{E}_{\infty}^{\text{tot}} = \mathbf{E}_{\infty}^{\text{inc}} + \mathbf{E}_{\infty}^{\text{sca}}$ and $\hat{\mathbf{r}}_{1,2}$ correspond to the two detection angles.

Finally, the geometric features of different structures lead to distinct spatial distributions of $\mathbf{J}^{\text{s}}$, which directly dictate the angular dependence of the far-field amplitudes (40) and thereby control the interference behavior in the two-photon correlation functions reported in this work.

III. Results

Following the theoretical derivations, the normalized two-photon correlation observables are fully determined by the complex far-field amplitudes at the detection directions. In the regime considered here, each incident single-photon wavepacket occupies a well-defined input spatial mode (channel) with a narrowband spectral envelope. For normally ordered photodetection correlations, the dependence on the quantum state enters only through the occupied input-mode operators, while the scattering from input channels to far-field detection modes is strictly linear. Therefore, the required transfer coefficients can be extracted from classical frequency-domain scattering simulations: for each excited input channel (incident direction and polarization), we compute the corresponding complex far-field at the detector directions, and then evaluate $g^{(2)}$ and $\tilde{N}_c$ using the closed-form expressions in Section II.

In this section, two representative scenarios are investigated: 1) two-photon scattering from a dielectric sphere, which exhibits angle-dependent HOM-type suppression of coincidences and 2) the generation of spatial–polarization entanglement mediated by a space-variant Pancharatnam–Berry phase (PBP) metasurface. In both cases, the structure acts as a distributed 3-D beam splitter: the effective "path amplitudes" are encoded in the continuous angular dependence of the far-field response rather than in discrete optical paths. Specifically, $\sigma = 1.2$ is adopted to facilitate the temporal visualization of the HOM dip. This choice ensures a clear representation of the coincidence features within the chosen time window, independent of the frequency-domain scattering calculations.

A. Dielectric Sphere

To study the joint detection probability, we consider two independent single-photon wavepackets injected into two orthogonal input channels: one is a y-polarized plane wave propagating along the x-direction ($\mathbf{k}_1 = k\mathbf{e}_x$), and the other is an x-polarized plane wave propagating along the y-direction ($\mathbf{k}_2 = k\mathbf{e}_y$). The detectors are placed in the far-field at directions (θ_1, ϕ_1) and (θ_2, ϕ_2), respectively.

To suppress the dominant co-polarized incident contribution in the detected signal and to isolate the scattered-field-induced correlations, we detect only the z-polarized component (i.e., $a = b = z$), following [24]. In the narrowband (degenerate) regime $\omega_{\mathbf{k}_1} \approx \omega_{\mathbf{k}_2} = \omega_0$, (18) reduces to

$$g_{zz}^{(2)}(\mathbf{r}_1, \mathbf{r}_2) = \frac{\omega_{k_1}\omega_{k_2}|E_{zk_1}(\mathbf{r}_1)\,E_{zk_2}(\mathbf{r}_2) + E_{zk_2}(\mathbf{r}_1)\,E_{zk_1}(\mathbf{r}_2)|^2}{\sum_{l=1,2}\omega_{k_l}|E_{zk_l}(\mathbf{r}_1)|^2\sum_{l=1,2}\omega_{k_l}|E_{zk_l}(\mathbf{r}_2)|^2}. \quad (42)$$

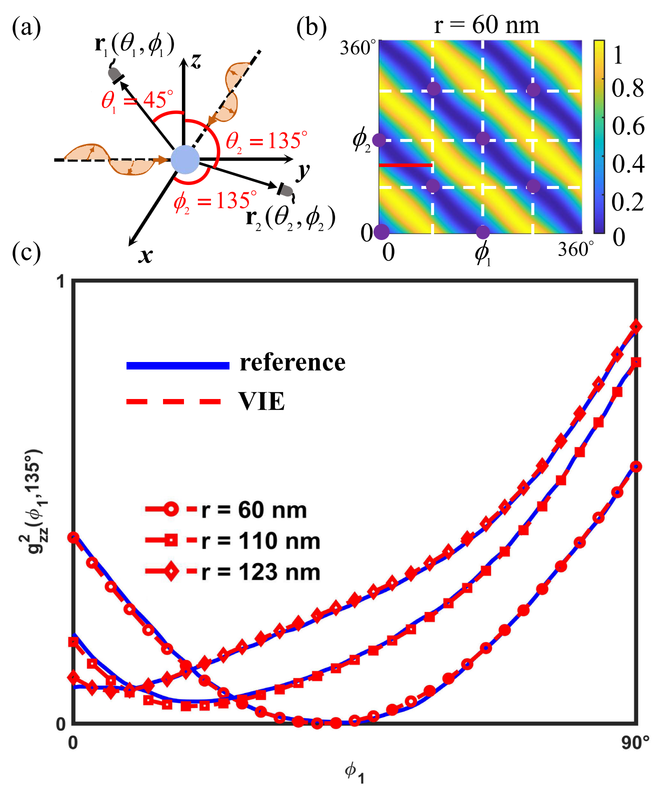

Fig. 2. (a) Schematic illustrating the two-photon state and the positions of detectors with respect to the dielectric sphere. (b) Normalized second-order correlation function $g_{zz}^{(2)}(\phi_1, \phi_2)$ for the sphere at $r = 60$ nm as a function of the azimuthal positions of the two detectors fixed at $\theta_1 = 45°, \theta_2 = 135°$. (c) Normalized second-order correlation function $g_{zz}^{(2)}(\phi_1, \phi_2 = 135°)$ for spheres with different radii $r = 60$, 110, and 123 nm.

Here, $E_{z\mathbf{k}_j}(\mathbf{r})$ denotes the detector-projected far-field complex amplitude at the observation direction corresponding to detector location $\mathbf{r}$, generated by the jth incident channel. Equation (42) explicitly shows that $g_{zz}^{(2)}$ is governed by the interference between the direct and exchange two-photon amplitudes, which vary continuously with observation angles.

1) Validation Against Analytical Reference: We validate the numerical method by comparing with the analytical results for an electrically small dielectric sphere reported in [24]. The sphere has relative permittivity $\varepsilon_r = 2.1$ at 750 THz. The two polar angles are fixed at $\theta_1 = 45°$ and $\theta_2 = 135°$, and the geometry and detector configuration are shown in Fig. 2(a). Using the VIE solution, the z-component of the far-field is computed via (40), and then $g_{zz}^{(2)}$ is evaluated by (42).

The red dashed curves in Fig. 2(c) show $g_{zz}^{(2)}(\phi_1, \phi_2)$ for $\phi_2 = 135°$ as a function of $\phi_1 \in [0°, 90°]$, corresponding to the detection arc highlighted in Fig. 2(b). For radii $r = 60$, 110, and 123 nm, the numerical results (red) agree well with the reference solution (blue), with relative ℓ_2 errors of 2.81%, 2.73%, and 1.59%, confirming the accuracy of the implementation.

Spheres of different radii induce substantial variations in the angular dependence of $g_{zz}^{(2)}$. The inset of Fig. 2(b) shows the full angular map over (ϕ_1, ϕ_2) for $r = 60$ nm. The blue diagonal stripes correspond to HOM-type destructive interference, that is, suppression of coincidences due to two-photon path

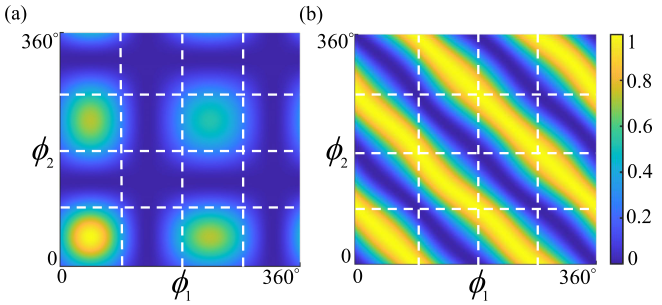

Fig. 3. Angular maps of normalized fourth-order field correlations. (a) Classical intensity-product correlation $P_{zz}^{(2)}$ (normalized). (b) Quantum normalized second-order correlation $g_{zz}^{(2)}$.

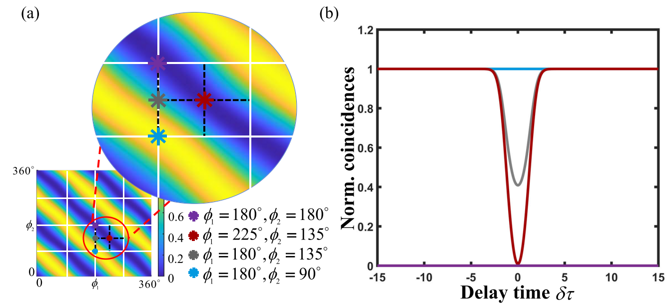

Fig. 4. (a) Four representative detection configurations on the angular map. (b) Normalized coincidence counts $\tilde{N}_c$ versus the controlled input delay $\delta\tau$ for these configurations. The Gaussian width parameter used for the temporal profile is $\sigma = 1.2$.

indistinguishability. The wide-angle persistence of the dip is attributed to the spherical symmetry and the dominance of a small number of scattering multipoles in the electrically small regime, which makes the relative complex amplitudes in (42) vary smoothly with angle and hence preserves the destructive-interference condition over extended angular regions. At the two detector positions marked by the purple symbols, one of the two path amplitudes vanishes because the corresponding far-field component is identically zero for one incident channel; this yields $g_{zz}^{(2)} = 0$ for a trivial single-path reason rather than genuine two-photon interference, as further clarified by the time-domain coincidence curves below.

2) Classical Fourth-Order Field Correlation for Comparison: For deterministic classical fields, a natural fourth-order field correlation is simply the product of intensities

$$P_{zz}^{(2)}(\mathbf{r}_1, \mathbf{r}_2) \triangleq I_z(\mathbf{r}_1)\, I_z(\mathbf{r}_2) = |E_z(\mathbf{r}_1)|^2 |E_z(\mathbf{r}_2)|^2 \tag{43}$$

where $E_z(\mathbf{r}) = E_{z\mathbf{k}_1}(\mathbf{r}) + E_{z\mathbf{k}_2}(\mathbf{r})$ is the coherent superposition of the two classical scattering responses. This classical quantity can be normalized (e.g., by its maximum over the scanned angles) and compared against the quantum $g_{zz}^{(2)}$ map. Fig. 3 contrasts the normalized classical fourth-order field correlation map with the quantum $g_{zz}^{(2)}$ map. The classical map is dominated by standard two-field interference fringes determined by second-order intensity coherence. In contrast, the quantum observable $g_{zz}^{(2)}$ encodes two-photon interference between direct and exchange amplitudes, leading to HOM-type suppression regions that have no direct classical analog under identical normalization.

3) Time-Domain Coincidence Curves: We further compute the normalized coincidence counts $\tilde{N}_c(\delta\tau)$ as a function of the controlled input delay $\delta\tau$ using (27)–(33). Based on the angular map in Fig. 2(b), four representative angular configurations are selected [Fig. 4(a)] with substantially different values of $g_{zz}^{(2)}$. Substituting the far-field complex amplitudes at these angles into the time-domain formulation yields the curves in Fig. 4(b).

The overall dip envelope is determined by the input wavepacket bandwidth (coherence time), while the dip visibility is governed by the spatially dependent two-path amplitudes in (42) (or equivalently, by A_{dir} and A_{ex}). In particular, configurations with strong destructive interference in the frequency-domain observable exhibit deep HOM dips at $\delta\tau = 0$ (red curve). When the two-photon interference is weak or absent (e.g., $g^{(2)} \approx 1$), the coincidence curve remains close to unity for all delays (blue curve). Importantly, the purple curve corresponds to a configuration where $g_{zz}^{(2)} = 0$ due to the vanishing of one path amplitude (a single-photon contribution at the detector) rather than two-photon interference; accordingly, $\tilde{N}_c(\delta\tau)$ stays suppressed for all $\delta\tau$, distinguishing it from a genuine HOM dip whose suppression is localized near $\delta\tau = 0$.

B. Dielectric Metasurfaces

Metasurfaces enable subwavelength control of amplitude, phase, polarization, and dispersion, with applications in flat optics [59], [60], holography [61], beam shaping, and polarization control. Recently, such capabilities have also been leveraged for manipulating quantum states of light [62], [63], [64].

Here we consider a polarization-converting metasurface based on a space-variant PBP profile, designed to deflect an incident plane wave into output directions at $\pm 10°$. For horizontally ($|H\rangle$) and vertically ($|V\rangle$) polarized inputs, the output polarization basis of interest is the left- and right-handed circular basis ($|L\rangle$, $|R\rangle$). At the operator level, it is convenient to express the corresponding mode creation operators via the circular-basis transformation

$$\hat{a}_L^\dagger = \frac{1}{\sqrt{2}}\left(\hat{a}_H^\dagger + i\,\hat{a}_V^\dagger\right), \quad \hat{a}_R^\dagger = \frac{1}{\sqrt{2}}\left(\hat{a}_H^\dagger - i\,\hat{a}_V^\dagger\right) \tag{44}$$

where the (spatial-mode) subscripts will be specified below.

The initial two-photon state is defined in a composite Hilbert space $\mathcal{H} = \mathcal{H}_a \otimes \mathcal{H}_b$, where a and b denote two orthogonal spatial input modes illuminating the metasurface. In this metasurface-assisted entanglement scheme, the relevant input is a polarization-entangled state in the circular basis

$$|\Psi_{\mathrm{in}}\rangle \propto \left(\hat{a}_{L,a}^\dagger \hat{a}_{L,b}^\dagger - e^{i\varphi}\hat{a}_{R,a}^\dagger \hat{a}_{R,b}^\dagger\right)|0\rangle \tag{45}$$

that is, a coherent superposition of the two alternatives "both photons are left-circular" and "both photons are right-circular" (the relative phase φ depends on the controlled input delay). This state is a NOON-like entangled state in the polarization degree of freedom.

A PBP metasurface acts as a polarization-dependent router: within the dominant ± 1 diffraction orders, the $|L\rangle$ and $|R\rangle$ components are deflected into two distinct far-field paths

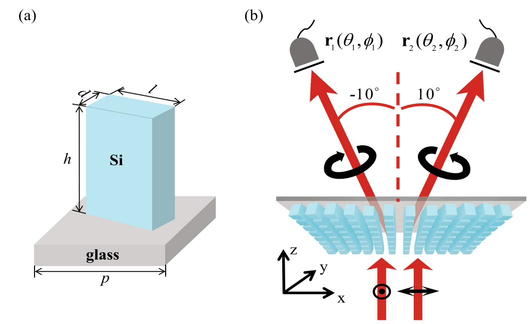

Fig. 5. (a) Geometric schematic of the metasurface unit cell. (b) Schematic of the two-photon state and the positions of detectors with respect to the PBP metasurface.

(angles) centered at + 10° and −10°, respectively. At the operator level, this routing can be modeled as

$$\hat{a}^{\dagger}_{L,a} \mapsto t_L\, \hat{c}^{\dagger}_{+},\ \hat{a}^{\dagger}_{L,b} \mapsto t_L\, \hat{c}^{\dagger}_{+},\ \hat{a}^{\dagger}_{R,a} \mapsto t_R\, \hat{c}^{\dagger}_{-},\ \hat{a}^{\dagger}_{R,b} \mapsto t_R\, \hat{c}^{\dagger}_{-} \quad (46)$$

where $\hat{c}^{\dagger}_{+}$ and $\hat{c}^{\dagger}_{-}$ create a photon in the two selected output spatial modes collected around + 10° and −10°, and $t_{L/R}$ are complex transfer coefficients (extracted from the full-wave simulation). Equation (46) assumes that the two input modes become indistinguishable within each selected diffraction channel, so that both a and b contribute coherently to the same output mode.

Applying (46) to (45) yields a path-NOON state in the selected far-field channels

$$\begin{aligned} |\Psi_{\text{out}}\rangle &\propto\ t_L^2 \left(\hat{c}^{\dagger}_{+}\right)^2 |0\rangle - e^{i\varphi} t_R^2 \left(\hat{c}^{\dagger}_{-}\right)^2 |0\rangle \\ &\propto\ \left(\left|2_+, 0_-\right\rangle - e^{i\varphi'} \left|0_+, 2_-\right\rangle\right) \end{aligned} \quad (47)$$

which is exactly the transformation "polarization NOON → path NOON" enabled by the metasurface-induced separation of circular polarizations. In the subsequent correlation analysis, the two detectors are aligned with the ±10° output channels, and the two-photon interference arises from the indistinguishability of the two-photon alternatives in (47).

For evaluating the normalized second-order correlation, we compute far-field projections onto circular polarization. Using the spherical transverse components (E_θ, E_ϕ), the left/right circular components are

$$E_L = \frac{1}{\sqrt{2}}\left(E_\theta + iE_\phi\right), \quad E_R = \frac{1}{\sqrt{2}}\left(E_\theta - iE_\phi\right). \quad (48)$$

Substituting the circularly polarized far-field amplitudes into (18) yields

$$\begin{aligned} &g^{(2)}_{LR}(\mathbf{r}_1, \mathbf{r}_2) \\ &= \frac{\omega_{k_H}\omega_{k_V} |E_{Rk_H}(\mathbf{r}_1) E_{Lk_V}(\mathbf{r}_2) + E_{Rk_V}(\mathbf{r}_1) E_{Lk_H}(\mathbf{r}_2)|^2}{\sum_{l=H,V} \omega_{k_l} |E_{Rk_l}(\mathbf{r}_1)|^2 \sum_{l=H,V} \omega_{k_l} |E_{Lk_l}(\mathbf{r}_2)|^2}. \end{aligned} \quad (49)$$

Referring to the structural parameters in [14], the PBP metasurface unit cell in Fig. 5(a) uses periodicity $p = 667$ nm, nanofin height $h = 830$ nm, length $l = 486$ nm, and width $d = 219$ nm. We assume refractive indices $n_{\text{Si}} = 3.44$ for silicon and $n_{\text{glass}} = 2.25$ for the substrate at wavelength 1550 nm. The local rotation angle follows the PBP design rule:

$$\theta_m = \frac{1}{2} k_0 \sin(\theta_t)\, m\, p \quad (50)$$

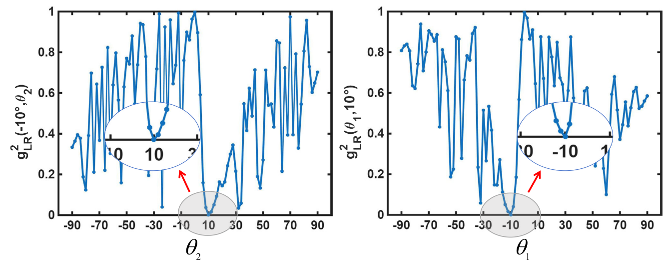

Fig. 6. (a) Normalized second-order correlation function $g^{(2)}_{LR}(\theta_1 = -10°, \theta_2)$ as a function of θ_2. (b) Normalized second-order correlation function $g^{(2)}_{LR}(\theta_1, \theta_2 = 10°)$ as a function of θ_1.

where $\theta_t = 10°$ is the desired deflection angle. This yields a rotation increment of 13.44° between adjacent unit cells. The metasurface consists of groups of 13 unit cells laterally, arranged into 7 × 7 groups along the x- and y-directions. It functions as a circular-polarization beam separator, deflecting $|R\rangle$ toward −10° and $|L\rangle$ toward +10°; the detection setup is shown in Fig. 5(b).

We simulate a structure of electrical size $40\lambda_0 \times 12\lambda_0 \times 2\lambda_0$ with a spatial discretization of 62 grids per λ_0, resulting in 18 013 710 mesh elements and 54 041 130 current unknowns. The dense VIE system is solved using FFT-accelerated MVM and BiCGStab with a parallel block preconditioner. Exploiting the structural regularity, the volume is partitioned into 7 × 7 blocks, and the preconditioned solves and FFT operations are executed in parallel on 24 threads [46]. The preconditioner reduces the solution time from 31.9 to 24 h.

The characteristic aperture dimension $D = 40\lambda_0$ gives a Fraunhofer distance $R_F \approx 2D^2/\lambda_0 = 3200\lambda_0$, which corresponds to ≈ 4.96 at 1550 nm. Since the correlation functions are evaluated at observation distances well beyond this threshold, the far-field approximation used in (40) is well satisfied, providing a reliable basis for evaluating $g^{(2)}$ observables.

Fixing the azimuthal angles at $\phi_1 = 180°$ and $\phi_2 = 0°$, Fig. 6(a) and (b) show $g^{(2)}_{LR}(\theta_1 = -10°, \theta_2)$ versus θ_2 and $g^{(2)}_{LR}(\theta_1, \theta_2 = 10°)$ versus θ_1, respectively. A vanishing correlation $g^{(2)}_{LR} = 0$ occurs at $\theta_1 = -10°$ and $\theta_2 = 10°$, indicating complete destructive two-photon interference (HOM suppression). The pronounced angular sensitivity of $g^{(2)}_{LR}$ highlights its utility as a two-photon probe of the metasurface scattering response.

We also compute the normalized coincidence counts $\tilde{N}_c(\delta\tau)$ at the vanishing-correlation configuration using (27). The results in Fig. 7 exhibit a characteristic HOM dip, consistent with the essential features reported in [14]. The simulated curve is smoother than experimental traces because we assume an idealized geometry and a quasimonochromatic Gaussian wavepacket, whereas experimental data are affected by fabrication tolerances, surface roughness, finite detector response, and background noise. Despite differences in fine-scale ripples, the dip visibility and delay dependence confirm that the proposed VIE-based framework captures the primary quantum interference behavior. As $\delta\tau$ increases and the photons become distinguishable, $\tilde{N}_c(\delta\tau)$ approaches unity, corresponding to the classical (distinguishable) limit.

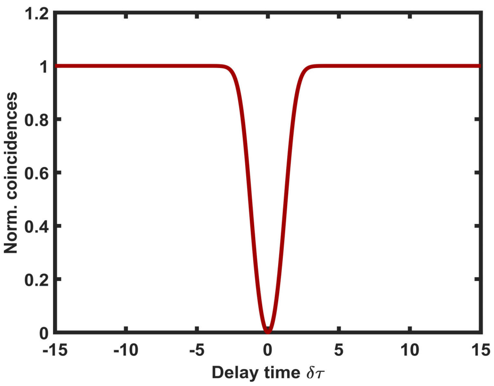

Fig. 7. Normalized coincidence counts $\tilde{N}_c$ between the two detection positions versus the controlled input delay $\delta\tau$. The Gaussian width parameter used for the temporal profile is $\sigma = 1.2$.

IV. Conclusion

This work investigates far-field two-photon interference associated with the HOM effect in arbitrary scattering environments. By combining a quantum photodetection formalism with full-wave CEM, we show that the normalized second-order correlation $g^{(2)}$ and the time-domain normalized coincidence $\tilde{N}_c(\delta\tau)$ can be evaluated directly from classical far-field complex amplitudes computed by a VIE-FFT solver. The key observation is that, for linear media, the mapping from incident channels (direction and polarization) to far-field detection modes is linear at the operator level; therefore, once the transfer coefficients are extracted from classical scattering simulations, the two-photon observables follow from normally ordered correlations.

For a lossless scatterer, the full input-output mapping between complete sets of asymptotic modes is described by a unitary multichannel scattering operator, which preserves the bosonic commutation relations. In our setting only two incident channels are populated and the observables are evaluated for two selected far-field detection modes; therefore the operator mapping can be projected onto this four-mode subspace, yielding an effective 2×2 input-to-output transfer relation whose elements are directly obtained from the full-wave computed far-field amplitudes and which leads to closed-form expressions for $g^{(2)}$ and $\tilde{N}_c(\delta\tau)$. The ultranarrowband assumption is used only to treat these transfer coefficients as approximately frequency-independent over the photon bandwidth, so that the temporal-delay dependence enters solely through the wavepacket overlap function.

Numerical results for a dielectric sphere and a PBP metasurface demonstrate pronounced angle-dependent HOM-type suppression of coincidences. The angular distribution of $g^{(2)}$ differs fundamentally from classical fourth-order field correlations, highlighting the genuinely two-photon nature of the interference. Moreover, the frequency-domain observable $g^{(2)}$ is quantitatively linked to the visibility and shape of the time-domain coincidence dip $\tilde{N}_c(\delta\tau)$, allowing one to distinguish true two-photon destructive interference from trivial zero-coincidence cases caused by vanishing single-path amplitudes. We further show that $g^{(2)}$ is highly sensitive to both structural dimensions and detection angles (e.g., sphere radius variations and metasurface angular scans), suggesting that far-field correlation measurements can serve as a diagnostic modality for retrieving material/structural information and detecting subtle perturbations in electromagnetic designs.

Future work will extend this framework to lossy and dispersive systems (where the scattering description must incorporate additional bath channels), and will explore correlation-enabled quantum inverse problems for complex electromagnetic structures, including multiangle coincidence measurements and optimization-driven design/inference using $g^{(2)}$-based objective functions.

References

[1] A. Blais, S. M. Girvin, and W. D. Oliver, “Quantum information processing and quantum optics with circuit quantum electrodynamics,” *Nature Phys.*, vol. 16, no. 3, pp. 247–256, Mar. 2020.

[2] M. A. Nielsen and I. L. Chuang, *Quantum Computation and Quantum Information.* Cambridge, U.K.: Cambridge Univ. Press, 2010.

[3] P. Kok, W. J. Munro, K. Nemoto, T. C. Ralph, J. P. Dowling, and G. J. Milburn, “Linear optical quantum computing with photonic qubits,” *Rev. Modern Phys.*, vol. 79, no. 1, pp. 135–174, Jan. 2007.

[4] M. O. Scully and M. S. Zubairy, *Quantum Optics*. Cambridge, U.K.: Cambridge Univ. Press, 1997.

[5] D.-Y. Na, J. Zhu, W. C. Chew, and F. L. Teixeira, “Quantum information preserving computational electromagnetics,” *Phys. Rev. A, Gen. Phys.*, vol. 102, no. 1, Jul. 2020, Art. no. 013711.

[6] W. C. Chew, B. Zhang, and J. Zhu, “Some selected unsolved problems in classical and quantum electromagnetics,” *Prog. Electromagn. Res.*, vol. 180, pp. 79–87, 2024.

[7] H. T. Dung, L. Knöll, and D.-G. Welsch, “Spontaneous decay in the presence of dispersing and absorbing bodies: General theory and application to a spherical cavity,” *Phys. Rev. A, Gen. Phys.*, vol. 62, no. 5, Oct. 2000, Art. no. 053804.

[8] S. Scheel, L. Knöll, and D.-G. Welsch, “Spontaneous decay of an excited atom in an absorbing dielectric,” *Phys. Rev. A, Gen. Phys.*, vol. 60, no. 5, pp. 4094–4104, Nov. 1999.

[9] P.-F. Qiao, W. E. I. Sha, W. C. H. Choy, and W. C. Chew, “Systematic study of spontaneous emission in a two-dimensional arbitrary inhomogeneous environment,” *Phys. Rev. A, Gen. Phys.*, vol. 83, no. 4, Apr. 2011, Art. no. 043824.

[10] M. E. Crenshaw, “Comparison of quantum and classical local-field effects on two-level atoms in a dielectric,” *Phys. Rev. A, Gen. Phys.*, vol. 78, no. 5, Nov. 2008, Art. no. 053827.

[11] T. G. Philbin, “Casimir effect from macroscopic quantum electrodynamics,” *New J. Phys.*, vol. 13, no. 6, Jun. 2011, Art. no. 063026.

[12] R. Bratschitsch and A. Leitenstorfer, “Artificial atoms for quantum optics,” *Nature Mater.*, vol. 5, no. 11, pp. 855–856, Nov. 2006.

[13] R. Dumke et al., “Roadmap on quantum optical systems,” *J. Opt.*, vol. 18, no. 9, Aug. 2016, Art. no. 093001.

[14] P. Georgi et al., “Metasurface interferometry toward quantum sensors,” *Light, Sci. Appl.*, vol. 8, no. 1, p. 70, Aug. 2019.

[15] G. Y. Slepyan, D. Mogilevtsev, I. Levie, and A. Boag, “Modeling of multimodal scattering by conducting bodies in quantum optics: The method of characteristic modes,” *Phys. Rev. Appl.*, vol. 18, no. 1, Jul. 2022, Art. no. 014024.

[16] W. C. Chew. (2016). *Quantum Mechanics Made Simple: Lecture Notes*. [Online]. Available: https://engineering.purdue.edu/wcchew/

[17] D. A. Miller, *Quantum Mechanics for Scientists and Engineers*. Cambridge, U.K.: Cambridge Univ. Press, 2008.

[18] K. Gottfried, *Quantum Mechanics, Volume I: Fundamentals*. Reading, MA, USA: Addison-Wesley, 1989.

[19] O. Lib and Y. Bromberg, “Quantum light in complex media and its applications,” *Nature Phys.*, vol. 18, no. 9, pp. 986–993, Sep. 2022.

[20] C. K. Hong, Z. Y. Ou, and L. Mandel, “Measurement of subpicosecond time intervals between two photons by interference,” *Phys. Rev. Lett.*, vol. 59, no. 18, pp. 2044–2046, Nov. 1987.

[21] S. Prasad, M. O. Scully, and W. Martienssen, “A quantum description of the beam splitter,” *Opt. Commun.*, vol. 62, no. 3, pp. 139–145, May 1987.

[22] D. Dzsotjan, B. Rousseaux, H. R. Jauslin, G. C. Des Francs, C. Couteau, and S. Guérin, “Mode-selective quantization and multimodal effective models for spherically layered systems,” *Phys. Rev. A, Gen. Phys.*, vol. 94, no. 2, Aug. 2016, Art. no. 023818.

[23] R. Gutiérrez-Jáuregui and R. Jáuregui, "Photons in the presence of parabolic mirrors," *Phys. Rev. A, Gen. Phys.*, vol. 98, no. 4, Oct. 2018, Art. no. 043808.

[24] P. Maurer, C. Gonzalez-Ballestero, and O. Romero-Isart, "Quantum electrodynamics with a nonmoving dielectric sphere: Quantizing Lorenz–Mie scattering," *J. Opt. Soc. Amer. B, Opt. Phys.*, vol. 40, no. 12, pp. 3137–3155, Nov. 2023.

[25] H. T. Dung, L. Knöll, and D.-G. Welsch, "Three-dimensional quantization of the electromagnetic field in dispersive and absorbing inhomogeneous dielectrics," *Phys. Rev. A, Gen. Phys.*, vol. 57, no. 5, pp. 3931–3942, May 1998.

[26] L. Novotny and B. Hecht, *Principles of Nano-Optics*. Cambridge, U.K.: Cambridge Univ. Press, 2012.

[27] S. Scheel and S. Buhmann, "Macroscopic quantum electrodynamics—Concepts and applications," *Acta Phys. Slovaca. Rev. Tuts.*, vol. 58, no. 5, pp. 675–809, Oct. 2008.

[28] G. S. Agarwal, *Quantum Optics*. Cambridge, U.K.: Cambridge Univ. Press, 2012.

[29] R. Bennett, T. M. Barlow, and A. Beige, "A physically motivated quantization of the electromagnetic field," *Eur. J. Phys.*, vol. 37, no. 1, Oct. 2015, Art. no. 014001.

[30] G. W. Hanson, "Aspects of quantum electrodynamics compared to the classical case: Similarity and disparity of quantum and classical electromagnetics," *IEEE Antennas Propag. Mag.*, vol. 62, no. 4, pp. 16–26, Aug. 2020.

[31] R. J. Garbacz, "Modal expansions for resonance scattering phenomena," *Proc. IEEE*, vol. 53, no. 8, pp. 856–864, Aug. 1965.

[32] R. Garbacz and R. Turpin, "A generalized expansion for radiated and scattered fields," *IEEE Trans. Antennas Propag.*, vol. AP-19, no. 3, pp. 348–358, May 1971.

[33] R. Garbacz and D. Pozar, "Antenna shape synthesis using characteristic modes," *IEEE Trans. Antennas Propag.*, vol. AP-30, no. 3, pp. 340–350, May 1982.

[34] R. Harrington and J. Mautz, "Theory of characteristic modes for conducting bodies," *IEEE Trans. Antennas Propag.*, vol. AP-19, no. 5, pp. 622–628, Sep. 1971.

[35] Y. Chen and C. F. Wang, *Characteristics Modes Theory and Applications in Antenna Engineering*. Hoboken, NJ, USA: Wiley, 2015.

[36] R. Harrington and J. Mautz, "Computation of characteristic modes for conducting bodies," *IEEE Trans. Antennas Propag.*, vol. AP-19, no. 5, pp. 629–639, Sep. 1971.

[37] K. Yee, "Numerical solution of initial boundary value problems involving Maxwell's equations in isotropic media," *IEEE Trans. Antennas Propag.*, vol. AP-14, no. 3, pp. 302–307, May 1966.

[38] J.-M. Jin, *The Finite Element Method in Electromagnetics*. Hoboken, NJ, USA: Wiley, 2015.

[39] A. Taflove and S. C. Hagness, *Computational Electromagnetics: The Finite-Difference Time-Domain Method*, 2nd ed., Norwood, MA, USA: Artech House, 2000.

[40] D.-Y. Na and W. C. Chew, "Quantum electromagnetic finite-difference time-domain solver," *Quantum Rep.*, vol. 2, no. 2, pp. 253–265, Apr. 2020.

[41] S. Savasta, O. Di Stefano, and R. Girlanda, "Light quantization for arbitrary scattering systems," *Phys. Rev. A, Gen. Phys.*, vol. 65, no. 4, Mar. 2002, Art. no. 043801.

[42] C. Forestiere and G. Miano, "Integral formulation of the macroscopic quantum electrodynamics in dispersive dielectric objects," *Phys. Rev. A, Gen. Phys.*, vol. 107, no. 6, Jun. 2023, Art. no. 063705.

[43] C. Forestiere, G. Gravina, G. Miano, G. Rubinacci, and A. Tamburrino, "Static surface mode expansion for the electromagnetic scattering from penetrable objects," *IEEE Trans. Antennas Propag.*, vol. 71, no. 8, pp. 6779–6793, Aug. 2023.

[44] G. Miano, L. M. Cangemi, and C. Forestiere, "Quantum emitter interacting with a dispersive dielectric object: A model based on the modified Langevin noise formalism," *Nanophotonics*, vol. 14, no. 23, pp. 4019–4027, Mar. 2025.

[45] A. Canaguier-Durand and R. Carminati, "Quantum coherence of light emitted by two single-photon sources in a structured environment," *Phys. Rev. A, Gen. Phys.*, vol. 93, no. 3, Mar. 2016, Art. no. 033836.

[46] C. Huang and W. E. I. Sha, "A parallel block preconditioner-based VIE-FFT algorithm for modeling the electromagnetic response from nanostructures," *IEEE Trans. Antennas Propag.*, vol. 72, no. 1, pp. 1051–1056, Jan. 2024.

[47] L. Mandel and E. Wolf, *Optical Coherence and Quantum Optics*. Cambridge, U.K.: Cambridge Univ. Press, 1995.

[48] R. H. Brown and R. Q. Twiss, "Interferometry of the intensity fluctuations in light—I. Basic theory: The correlation between photons in coherent beams of radiation," *Proc. Roy. Soc. London. Ser. A. Math. Phys. Sci.*, vol. 242, no. 1230, pp. 300–324, Nov. 1957.

[49] R. J. Glauber, "The quantum theory of optical coherence," *Phys. Rev.*, vol. 130, no. 6, pp. 2529–2539, Jun. 1963.

[50] C. Chen et al., "Wavelength-tunable high-fidelity entangled photon sources enabled by dual Stark effects," *Nature Commun.*, vol. 15, no. 1, p. 5792, Jul. 2024.

[51] H. J. Kimble, M. Dagenais, and L. Mandel, "Photon antibunching in resonance fluorescence," *Phys. Rev. Lett.*, vol. 39, no. 11, pp. 691–695, Sep. 1977.

[52] G. Messin, J. P. Hermier, E. Giacobino, P. Desbiolles, and M. Dahan, "Bunching and antibunching in the fluorescence of semiconductor nanocrystals," *Opt. Lett.*, vol. 26, no. 23, pp. 1891–1893, Dec. 2001.

[53] R. Carminati, G. Cwilich, L. S. Froufe-Pérez, and J. J. Sáenz, "Speckle fluctuations resolve the interdistance between incoherent point sources in complex media," *Phys. Rev. A, Gen. Phys.*, vol. 91, no. 2, Feb. 2015, Art. no. 023807.

[54] W. C. Chew, *Waves and Fields in Inhomogenous Media*. Hoboken, NJ, USA: Wiley, 1999.

[55] L. Knoll, S. Scheel, and D.-G. Welsch, "QED in dispersing and absorbing media," 2000, *arXiv:quant-ph/0006121*.

[56] C. Viviescas and G. Hackenbroich, "Field quantization for open optical cavities," *Phys. Rev. A, Gen. Phys.*, vol. 67, no. 1, Jan. 2003, Art. no. 013805.

[57] R. F. Harrington, *Field Computation by Moment Methods*. Hoboken, NJ, USA: Wiley, 1993.

[58] H. A. van der Vorst, "Bi-CGSTAB: A fast and smoothly converging variant of bi-CG for the solution of nonsymmetric linear systems," *SIAM J. Sci. Stat. Comput.*, vol. 13, no. 2, pp. 631–644, Mar. 1992.

[59] M. Khorasaninejad, W. T. Chen, R. C. Devlin, J. Oh, A. Y. Zhu, and F. Capasso, "Metalenses at visible wavelengths: Diffraction-limited focusing and subwavelength resolution imaging," *Science*, vol. 352, no. 6290, pp. 1190–1194, Jun. 2016.

[60] S. Wang et al., "A broadband achromatic metalens in the visible," *Nature Nanotechnol.*, vol. 13, no. 3, pp. 227–232, Jan. 2018.

[61] L. Huang et al., "Three-dimensional optical holography using a plasmonic metasurface," *Nature Commun.*, vol. 4, no. 1, p. 2808, Nov. 2013.

[62] L. Li et al., "Metalens-array–based high-dimensional and multiphoton quantum source," *Science*, vol. 368, no. 6498, pp. 1487–1490, Jun. 2020.

[63] T. Stav et al., "Quantum entanglement of the spin and orbital angular momentum of photons using metamaterials," *Science*, vol. 361, no. 6407, pp. 1101–1104, Sep. 2018.

[64] K. M. A. Yousef, M. D'Alessandro, M. Yeh, N. Sinclair, M. Loncar, and F. Capasso, "Metasurface quantum graphs for generalized hong-ou-mandel interference," *Science*, vol. 389, no. 6758, pp. 416–422, Jul. 2025.

Chengnian Huang (Student Member, IEEE) received the B.Eng. degree in electronic science and technology from Xiamen University, Xiamen, China, in 2020. She is currently pursuing the Ph.D. degree in electronic science and technology with Zhejiang University, Hangzhou, China.

From April 2024 to October 2024, she was a Visiting Ph.D. Student at the Department of Electrical and Electronic Engineering, The Hong Kong Polytechnic University, Hong Kong. Her research interests include the method of moments, volume integral equation method, finite-difference frequency-domain method, electromagnetic simulation of micro–nanostructures, and quantum scattering.

Hangyu Ge received the B.E. degree from the School of Information Science and Engineering, Shandong University, Jinan, China, in 2022. He is currently pursuing the Ph.D. degree with the College of Information Science and Electronic Engineering, Zhejiang University, Hangzhou, China.

His research interests include single-photon sources and entangled photon sources based on semiconductor quantum dots.

Yijia Cheng received the B.Eng. degree in electronic information science and technology from Chongqing University, Chongqing, China, in 2021. She is currently pursuing the Ph.D. degree in electronic science and technology with Zhejiang University, Hangzhou, China.

Her research interests include computational nanophotonics, scattering matrix method, Fourier modal method, and higher-order topological photonics.

Zi He (Senior Member, IEEE) was born in Hebei, China. She received the B.Sc. and Ph.D. degrees in electronic information engineering from the School of Electrical Engineering and Optical Technique, Nanjing University of Science and Technology (NJUST), Nanjing, China, in 2011 and 2016, respectively.

She was a Visiting Scholar with the University of Illinois at Urbana–Champaign (UIUC), Champaign, IL, USA, from September 2015 to 2016. She was a Post-Doctoral Researcher at the Science and Technology on Electromagnetic Scattering Laboratory, Beijing Institute of Environmental Features (BIEF), Beijing, China, from 2017 to 2020. She is currently an Associate Professor with the Department of Communication Engineering, NJUST. Her research interests include antennas, RF-integrated circuits, and computational electromagnetics.

Feng Liu received the bachelor's degree from Yantai University, Yantai, China, in 2008, the master's degree from the University of Sheffield, Sheffield, U.K., in 2009, and the Ph.D. degree from TU Dortmund, Dortmund, Germany, in 2013.

He was a Post-Doctoral Research Fellow at the University of Sheffield and RWTH Aachen University, Aachen, Germany, from 2013 to 2019. In 2019, he joined the College of Information Science and Electronic Engineering, Zhejiang University, Hangzhou, China, where he is currently a tenured Associate Professor. His research focuses on quantum light sources based on III–V quantum dots, cavity/waveguide-QED, and integrated quantum optical circuits.

Wei E. I. Sha (Fellow, IEEE) received the Ph.D. degree in electromagnetic fields and microwave technology from Anhui University, Hefei, China, in 2008.

From 2008 to 2017, he was with the Department of Electrical and Electronic Engineering, University of Hong Kong, where he served as a Post-Doctoral Research Fellow and later as a Research Assistant Professor. From 2018 to 2019, he was a Marie Skłodowska-Curie Individual Fellow at University College London, U.K. He is currently a Tenured Associate Professor with the College of Information Science and Electronic Engineering, Zhejiang University, Hangzhou, China, where he serves as the Deputy Director of the Institute of Electromagnetic Information and Electronic Integration. His works have been cited over 13,770 times on Google Scholar with an h-index of 62. He has authored or co-authored two books, 10 book chapters, and over 220 peer-reviewed journal articles. His research interests include theoretical and applied electromagnetics, with a focus on computational electromagnetics, quantum electromagnetics, and electromagnetic information theory.

Dr. Sha received the ACES Technical Achievement Award in 2022, the Second Prize of Science and Technology Award of the China Institute of Communications in 2024, the Second Prize for Science and Technology from the Anhui Provincial Government in 2015, and 11 international conference paper awards. He served as an Associate Editor for the IEEE JOURNAL ON MULTISCALE AND MULTIPHYSICS COMPUTATIONAL TECHNIQUES, the IEEE *Open Journal of Antennas and Propagation, and Electromagnetic Science*. He is the Founding Chair of the IEEE Antennas and Propagation Society (AP-S) Zhejiang Chapter.